phys. stat. sol. (a) **174**, 413 (1999)

Subject classification: 72.40.+w; 73.40.Kp; S7.13; S7.15

The Analysis of the Performance for P–p–n and N–n–p Hetero- and Homojunction GaSb/$Ga_{0.8}In_{0.2}As_{0.19}Sb_{0.81}$ Photodetectors

YUAN TIAN[1]), BAOLIN ZHANG, TIANMING ZHOU, HONG JIANG, and YIXIN JIN

Changchun Institute of Physics, Chinese Academy of Sciences, Changchun 130021, People's Republic of China

(Received March 22, 1999; in revised form June 14, 1999)

In this paper, the performance is analyzed for the P_1–p_2–n and N_1–n_2–p hetero- and homojunction GaSb/$Ga_{0.8}In_{0.2}As_{0.19}Sb_{0.81}$ photodetectors operated at 300 K, based on the incident wavelength and the parameters of GaSb and $Ga_{0.8}In_{0.2}As_{0.19}Sb_{0.81}$. The analyzed results show that the detectivity is much higher with the light incident first through the p-type than first through the n-type $Ga_{0.8}In_{0.2}As_{0.19}Sb_{0.81}$ for both structures. In addition, the carrier concentration of GaSb should be as low as possible to reduce the tunneling noise through the P_1–p_2 and N_1–n_2 heterojunctions. With the same condition for the two structures, the N_1–n_2–p structure is more advantage than the P_1–p_2–n structure because the high P_1–p_2 heterojunction recombination velocity increases the Auger and radiative noise mechanisms, which limit the performance of photodetectors.

1. Introduction

Photodetectors operating in the 1 to 3, 3 to 5, and 8 to 12 μm atmospheric windows have a variety of commercial applications in air pollution and industrial process control, automobile emission monitoring, and future lightwave communication systems using novel fiber materials [1 to 3]. HgCdTe (MCT) has been the dominate material system for these applications [4 to 6]. However, it suffers from the problem of instability and non-uniformity growth. There has been much interest in the use of the GaInAsSb quaternary alloy system as an alternative to MCT driven by the advanced material growth and processing technology. This quaternary alloy system will provide room temperature IR detectors adjustable over the 1.7 to 4.5 μm wavelength range [7, 8]. With proper device design, both the cut-on and cut-off wavelength can be tailored. A significant advantage of using quaternary systems over binary and ternary compounds is the ability to "tune" the bandgap while still providing the lattice-matched growth to the substrate material. Another expected advantage is that this detector structure will give a good detectivity at room temperature, while most commercially available detectors require cooling to liquid nitrogen temperature.

The performance of GaInAsSb detectors is limited by noise mechanisms and the quantum efficiency. In previous papers, the detectivity related with the above two factors for p–n homojunction detectors operated at room temperature have been discussed in detail [9 to 11]. Moreover, the performance of the p^+–p–n and n^+–n–p

[1]) Corresponding author: Tel.: 86-431-5952215 ext.232; Fax: 86-431-5955378;
e-mail: snmocvd@public.cc.jl.cn

GaInAsSb photodetectors is also reported [12]. For the three-layer structure, the detectivity has much improvement compared to that for the two-layer structure, because the incident photons can be sufficiently absorbed for the three-layer structure and the quantum efficiency is increased. In addition, the interface recombination at the isotype homojunction (p^+–p or n^+–n junction) is reduced by the heavily doped layer, which is useful to improve the detector performance. Based on the above considerations, in this paper the performance of the P–p–n and N–n–p hetero- and homojunction $GaSb/Ga_{0.8}In_{0.2}As_{0.19}Sb_{0.81}$ detectors is analyzed, in which the $Ga_{0.8}In_{0.2}As_{0.19}Sb_{0.81}$ material is lattice-matched to the GaSb material. (The capital letters represent the wide bandgap materials and the small letters represent the narrow bandgap materials.) When using a wide bandgap material as epitaxial layer, the cut-on and cut-off wavelengths can be tailored because the wide bandgap material is considered as a window layer, in which the high-energy photons are absorbed by the wide bandgap material, while the low-energy photons cross the wide bandgap material and are absorbed by the narrow bandgap material near the heterointerface, which is useful to select the working-wavelength for detectors. In the n–p homojunction, four kinds of noise mechanism are considered: the Auger and radiative mechanisms in the n- and p-regions, the generation–recombination (GR) mechanism in the n–p depletion region and the direct-band tunneling through the n–p depletion region [11]. In addition, in the

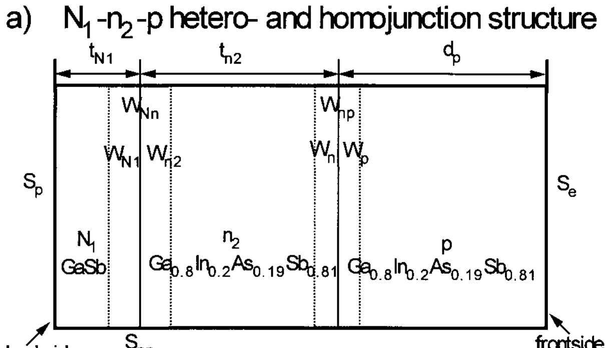

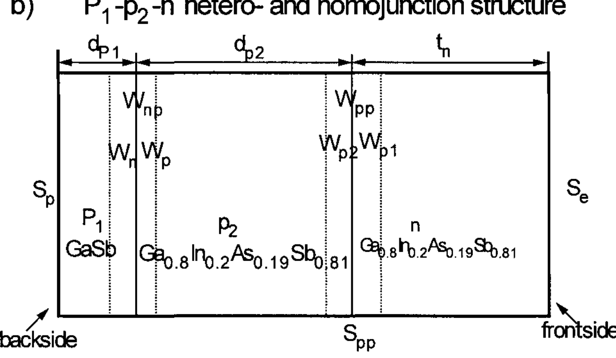

Fig. 1. The structures for N_1–n_2–p and P_1–p_2–n hetero- and homojunction $GaSb/Ga_{0.8}In_{0.2}As_{0.19}Sb_{0.81}$ photodetectors

Table 1
Tunneling current in the N–n and P–p heterojunction

	N–n	P–p
energy band profile		
tunneling current	$J_{s_N} = A^* T^2 P_N \exp\left(-\frac{qV_{d_N} + \delta_N}{KT}\right)$ $E_{min} = \max\,[E_c(0^+),\ E_c(W_N)]$	$J_{s_P} = A^* T^2 P_P \exp\left(-\frac{qV_{d_2} + \delta_2}{KT}\right)$ $E_{max} = \min\,[E_V(0^-),\ E_V(W_2)]$

N–n and P–p isotype heterojunctions, besides the GR mechanism, the heterojunction tunneling mechanism is an important noise mechanism to effect the detector performance.

2. Theoretical Analysis

The GaSb/GaInAsSb structure can be fabricated as either a frontside or backside illuminated detector. Fig. 1 shows the structures for N_1-GaSb/n_2-$Ga_{0.8}In_{0.2}As_{0.19}Sb_{0.81}$/p-$Ga_{0.8}In_{0.2}As_{0.19}Sb_{0.81}$ and P_1-GaSb/p_2-$Ga_{0.8}In_{0.2}As_{0.19}Sb_{0.81}$/n-$Ga_{0.8}In_{0.2}As_{0.19}Sb_{0.81}$ photodetectors, respectively. At the N–n and P–p heterointerfaces, the energy bands are discontinued, and spikes and notches appear. The effective wavelength is in the range of 1.7 to 2.5 μm. The incident light is from the GaSb surface or from the GaInAsSb surface, which is defined as the back- or frontside illuminated case, respectively. The figure of merit used to characterize the sensitivity of photodetectors is the detectivity D^*, which is dependent on the wavelength of the incident light λ, the quantum efficiency η and the zero-bias persistence product R_0A,

$$D^* = \frac{q\eta\lambda}{hc}(R_0A/4KT)^{1/2}\,. \tag{1}$$

R_0A can be expressed by $R_0A = KT/qJ_s$, and J_s is the noise saturated current.

The detail for the noise mechanisms and the quantum efficiency is shown in the appendix (see also Table 1).

3. Results and Discussions

In this paper, the R_0A, quantum efficiency (η) and detectivity (D^*) are calculated and analyzed for P_1-GaSb/p_2-$Ga_{0.8}In_{0.2}As_{0.19}Sb_{0.81}$/n-$Ga_{0.8}In_{0.2}As_{0.19}Sb_{0.81}$ and N_1-GaSb/n_2-$Ga_{0.8}In_{0.2}As_{0.19}Sb_{0.81}$/p-$Ga_{0.8}In_{0.2}As_{0.19}Sb_{0.81}$ photodetectors operated at 300 K. The incident light is from the GaSb surface or from the $Ga_{0.8}In_{0.2}As_{0.19}Sb_{0.81}$ surface with an ideal state, in which all photons with the energy lower than the material bandgap are assumed to cross this material and to reach the next material without any loss. That is, the weakening of the incident light due to impurity absorption and lattice scattering etc. is neglected. The basic parameters are listed in Table 2 and the related parameters have been shown in Ref. [9].

Table 2
Basic parameters for the P_1–p_2–n and N_1–n_2–p hetero- and homo-junction structures

basic parameters	T = 300 K, $N_f = 10^{14}$ cm^{-3}, $\sigma_s = 10^{-15}$ cm^2					
	P_1–p_2–n structure			N_1–n_2–p structure		
	P_1-region	p_2-region	n-region	N_1-region	n_2-region	p-region
carrier concentration (cm^{-3})	10^{16}	10^{17}	10^{18}	10^{16}	10^{18}	10^{17}
width (μm)	0.5	5	2	0.5	2	5
mobility (cm^2/Vs)	240	240	1000	1000	1000	240
surface recombination velocity (m/s)	0		0	0		0

Fig. 2 shows the detectivity as a function of the incident light wavelength for P_1–p_2–n and N_1–n_2–p structures in both the front- and backside illuminated cases, with other parameters in Table 2 keeping constants. On the assumption that the photons with energy lower than $E_{g,GaSb}$ all cross GaSb without any weakening, the main absorption appears in the $Ga_{0.8}In_{0.2}As_{0.19}Sb_{0.81}$ p–n homojunction. Based on the bandgap of GaSb and $Ga_{0.8}In_{0.2}As_{0.19}Sb_{0.81}$, the cut-on and cut-off wavelengths are 1.7 and 2.5 μm, respectively. A similar phenomenon is shown in the two parts of Fig. 2. High detectivity can be obtained with the photons first absorbed in the p-$Ga_{0.8}In_{0.2}As_{0.19}Sb_{0.81}$ material. As we know, the minority carrier diffusion is caused by the photons incident into the material. In the p-type material, the electrons being minority carriers have high diffu-

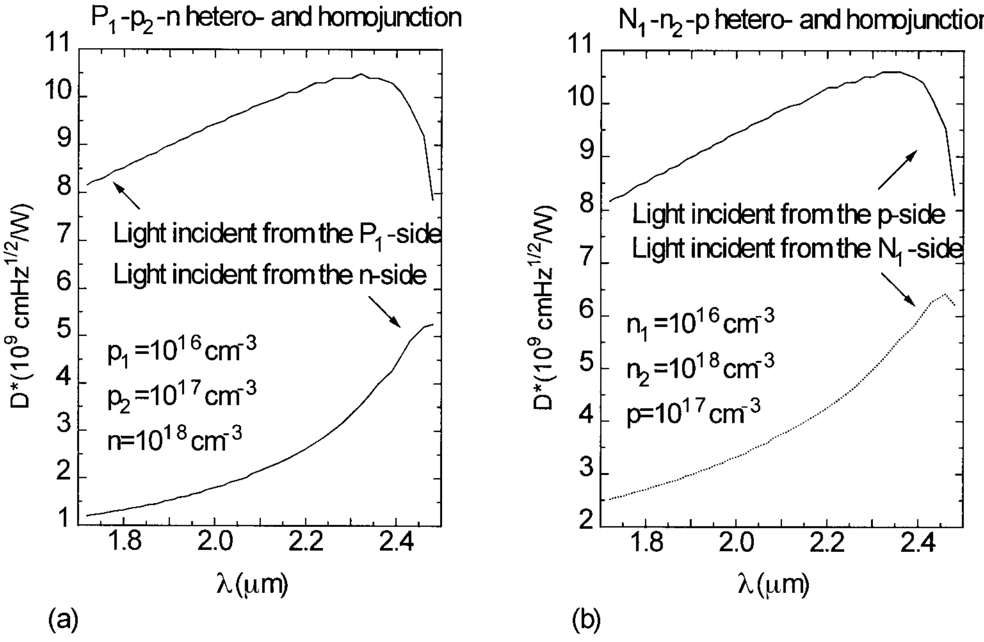

Fig. 2. The dependence of the detectivity on the incident light wavelength (λ) with both the front- and backside illuminated cases operated at 300 K for the P_1–p_2–n and N_1–n_2–p structures

sion velocity (embodied by the mobility) and high diffusion length, which makes electrons absorbed sufficiently before recombined, under the condition of the width of the p-type material shorter than the diffusion length. On the contrary, in the n-type material, the holes being minority carriers have low diffusion velocity and diffusion length, and most of the holes are recombined before being absorbed. Therefore, for our discussed structures, the main absorption is in the p-type $Ga_{0.8}In_{0.2}As_{0.19}Sb_{0.81}$ material. When the light through the n-type $Ga_{0.8}In_{0.2}As_{0.19}Sb_{0.81}$ reaches the p-type $Ga_{0.8}In_{0.2}As_{0.19}Sb_{0.81}$, the light intensity is reduced, which makes the absorption in the p-side decreased and the detectivity weakened simultaneously.

The maximum value of D^* is obtained at $\lambda = 2.32$ μm for the N_1–n_2–p structure with the frontside illuminated case and for the P_1–p_2–n structure with the backside illuminated case. In the following, the detectivity for the above two cases is calculated at $\lambda = 2.32$ μm. Because the absorption of incident photons is in the n–p homojunction, and as we know that all kinds of noise mechanism are independent, the influence of the parameters in n- and p-side $Ga_{0.8}In_{0.2}As_{0.19}Sb_{0.81}$ material on the performance of these two structure detectors is the same as that one for the n–p homojunction structure analyzed in a previous paper [11]. For the two mentioned structures, therefore, in this paper only the influence (on R_0A, η and detectivity) of the parameters in the wide bandgap GaSb material is discussed in detail.

3.1 P_1-GaSb/p_2-$Ga_{0.8}In_{0.2}As_{0.19}Sb_{0.81}$/n-$Ga_{0.8}In_{0.2}As_{0.19}Sb_{0.81}$ hetero- and homojunction structure with the backside illuminated case

Fig. 3 shows R_0A and η as well as their corresponding components as a function of the p_2-side carrier concentration (p_2) with other parameters in Table 2 keeping constants. In Fig. 3a, because of the lower carrier concentration of P_1-GaSb, the hole tunneling through the P_1–p_2 heterojunction does not appear. Except for the GR mechanism, in the P_1–p_2 heterojunction other noise mechanisms are similar to those in the n–p homojunction structure [11]. The high carrier concentration in each layer improves $(R_0A)_{GR}$, but at the same time the tunneling mechanism strongly reduces R_0A. In Fig. 3b, because the main absorption for the incident photons is in the p-type material, the quantum efficiency is limited by its component in this region, while its other components almost do not contribute to the quantum efficiency, which decides that the parameters in the p-side and related ones will have much influence on the detectivity.

The dependence of R_0A, η and D^* on p_2 is shown in Fig. 4 with the P_1-side surface recombination velocity (S_e) as a parameter, moreover $(R_0A)_{Auger}$ and $(R_0A)_{Rad}$ are also plotted in Fig. 4a. Although η is reduced with high S_e, which decreases D^*, the shape of D^* is limited by R_0A. The high S_e via the heterointerface recombination velocity S_{pp} has strong influence on the performance of photodetectors, which is not expected. For the p^+–p–n structure, the influence of the p^+-side surface recombination velocity is limited via S_{pp}, which is useful to suppress the noise and to improve the detectivity [12]. However, for the P_1–p_2–n hetero- and homojunciton structure, S_e is not limited by S_{pp}; on the contrary, S_{pp} is improved with high S_e. In order to show the influence of S_e on S_{pp}, Fig. 5 shows their relationship with the P_1-side width (d_{P1}) as a parameter, keeping $p_1 = 10^{16}$ cm^{-3} and $p_2 = 10^{17}$ cm^{-3}. In this figure, at $d_{P1} = 0.5$ μm, S_{pp} is much higher than S_e in the range of $S_e < 10^6$ m/s, which is caused by the low p_1 because of $S_{pp} \propto 1/p_1$. S_e via S_{pp} affects the Auger and radiative mechanisms and η. With high S_e, the Auger

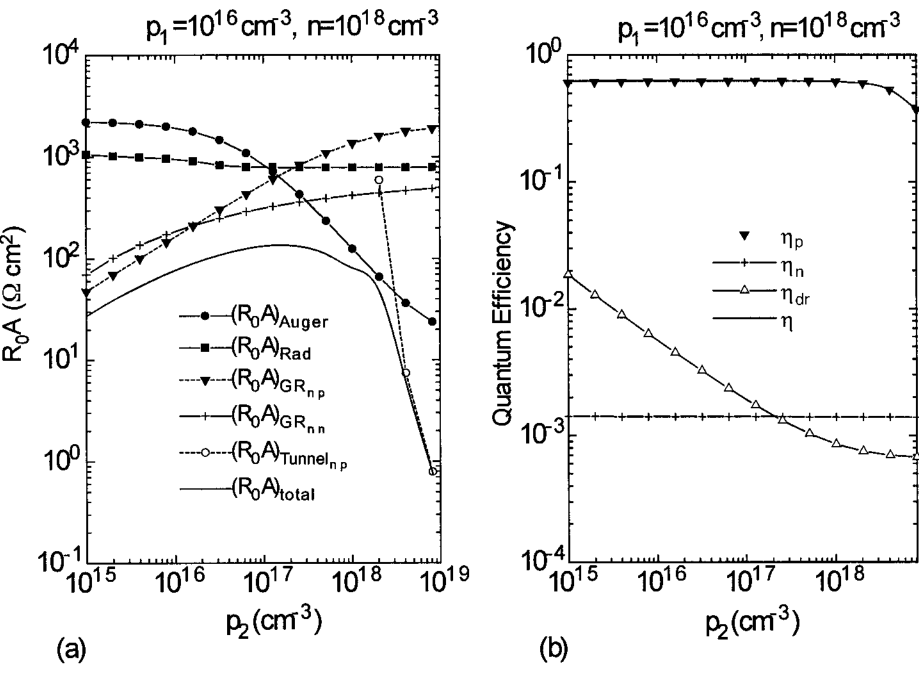

Fig. 3. The dependence of R_0A and η on the p_2-side carrier concentration (p_2) operated at 300 K for the P_1–p_2–n structure

and radiative mechanisms become the main noise mechanisms to decrease R_0A (seen in Fig. 4a), moreover η also decreases, both of which affect the improvement of the detectivity. This result shows that the high P_1-side carrier concentration is necessary to reduce S_{pp} at the P_1–p_2 isotype heterojunction in order to improve the detectvity. In the range of $S_e < 10^2$ m/s, S_{pp} is increased with high d_{P1}, from which is clearly obtained that D^* will be reduced with high d_{P1} while keeping $S_e < 10^2$ m/s.

Fig. 6 shows the dependence of R_0A and D^* as well as $(R_0A)_{\text{Tunnel}_{pp}}$ on p_2 with the change of the P_1-side carrier concentration (p_1). With increasing p_1, the hole tunneling through the P_1–p_2 heterojunction strongly affects R_0A because with increasing p_1, the barrier decreases with reducing the build-in field and the width of the depletion region, which makes the hole tunneling rate large. D^* is limited by R_0A, therefore the decreasing of R_0A must reduce D^*. There exists a contradiction between the diffusion (including Auger and radiative mechanisms) and tunneling mechanisms. On the one hand, in order to suppress the Auger and radiative mechanisms, it is required to have a lower heterointerface recombination velocity that can be obtained by the higher P_1-side carrier concentration. On the other hand, the low P_1-side carrier concentration is necessary to reduce the hole tunneling rate, which can suppress the tunneling mechanism. However, for the p^+–p–n homojunciton structure, this contradiction can be avoided because the tunneling mechanism does not exist through the p^+–p homojunction. The high p^+-side carrier concentration reduces S_{pp}, which suppresses Auger and radiative mechanisms to improve D^* [12]. In Fig. 6, at $p_1 = 10^{16}$ cm^{-3}, the hole tunneling does not appear, and at $p_1 = 10^{17}$ cm^{-3}, the hole tunneling occupies the most range of p_2,

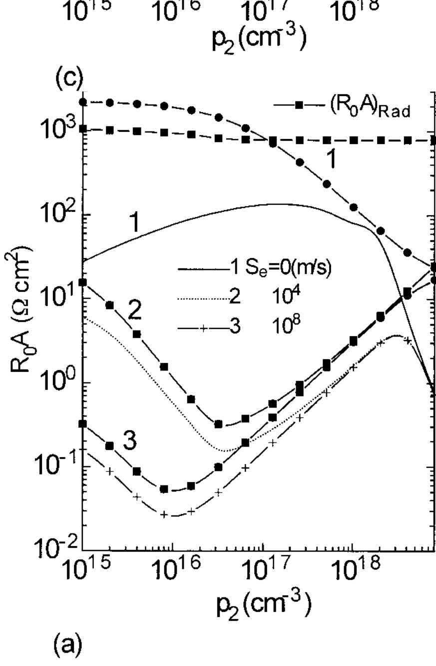

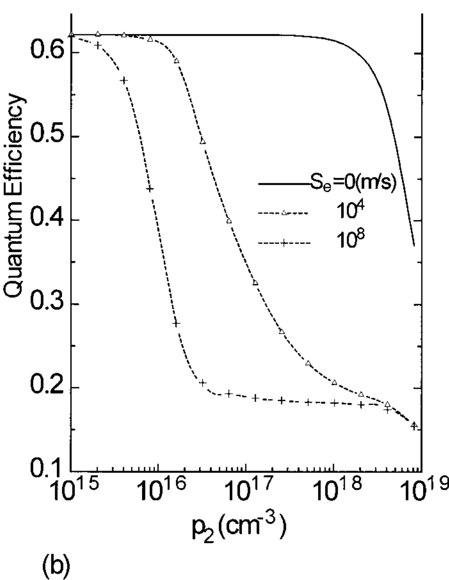

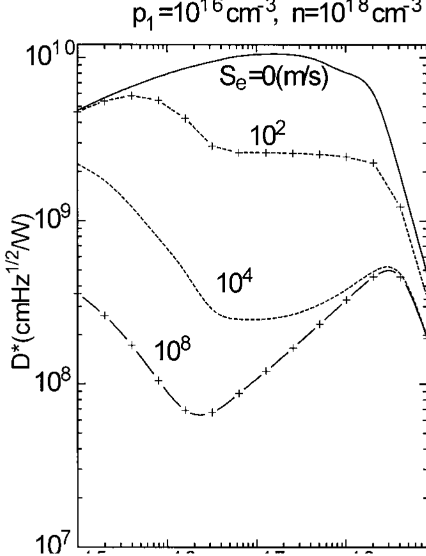

Fig. 4. The dependence of R_0A, η and D^* on the p_2-side carrier concentration (p_2) with the P_1-side surface recombination velocity (S_e) as a parameter operated at 300 K for the P_1–p_2–n structure

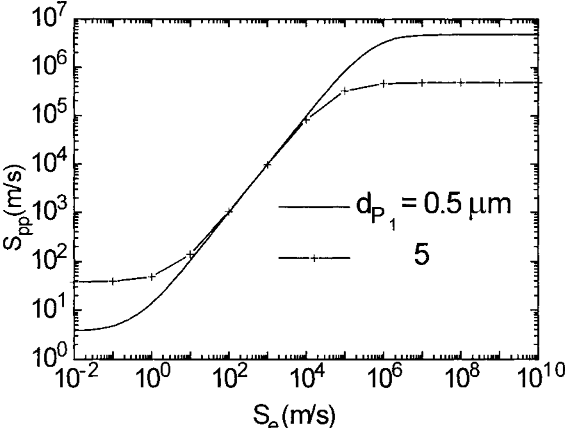

Fig. 5. The relation between the P_1–p_2 interface recombination velocity (S_{pp}) and the P_1-side surface recombination velocity (S_e) with the P_1-side width (d_{P1}) as a parameter operated at 300 K

but there is a little range of p_2 to obtain the optimum values for D^*. However, at $p_1 = 10^{18}$ cm^{-3}, both R_0A and D^* are limited by the hole tunneling and reduced. In addition, there exits a point of inflection on R_0A and D^* at $p_2 = 8 \times 10^{15}$ cm^{-3}, because the build-in field at the P_1–p_2 heterojunction has a change from $V_{dpp} < 0$ to $V_{dpp} > 0$ at this point.

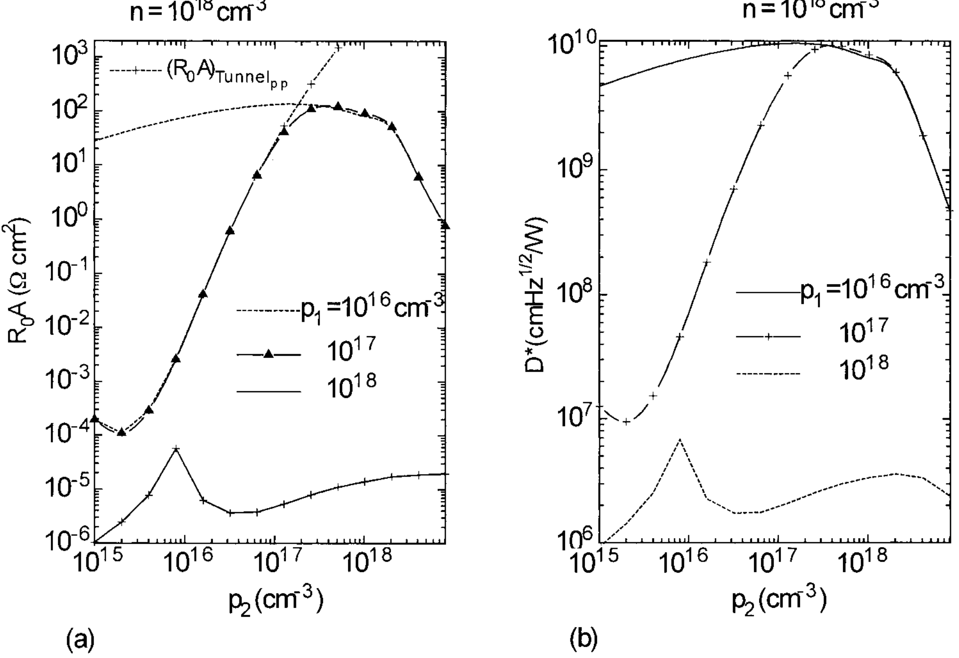

Fig. 6. The dependence of R_0A and D^* on the p_2-side carrier concentration (p_2) with the P_1-side carrier concentration (p_1) as a parameter operated at 300 K for the P_1–p_2–n structure

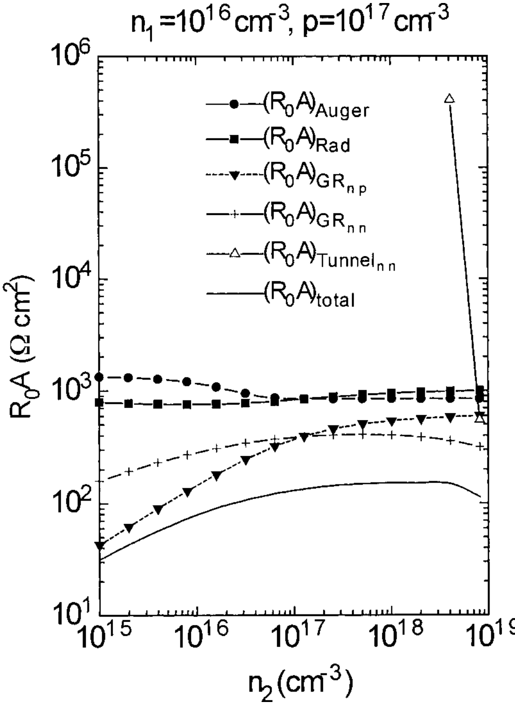

Fig. 7. The dependence of R_0A on the n_2-side carrier concentration (n_2) operated at 300 K for the N_1–n_2–p structure

3.2 N_1-GaSb/n_2-$Ga_{0.8}In_{0.2}As_{0.19}Sb_{0.81}$/ p-$Ga_{0.8}In_{0.2}As_{0.19}Sb_{0.81}$ hetero- and homojunction structure with the front-side illuminated case

The dependence of R_0A and its components on the n_2-side carrier concentration (n_2) is shown in Fig. 7. The direct-band tunneling through the n–p homojunction does not appear because of the low carrier concentration in the p-side ($p < 10^{18}$ cm^{-3}), while the electron tunneling through the N_1–n_2 heterojunction appears – but the tunneling current is so low that this noise mechanism almost does not affect R_0A. In addition, the Auger and radiative noise mechanisms are not the main noise mechanisms to limit R_0A.

Fig. 8 shows R_0A and D^* as a function of the n_2-side carrier concentration (n_2) with the N_1-side carrier concentration (n_1) as a parameter. Moreover, $(R_0A)_{\mathrm{Tunnel_{nn}}}$ with the change of n_1 is also plotted in Fig. 8a. The results in Fig. 8 are similar to those in Fig. 6. With increasing n_1, the electron tunneling strongly reduces R_0A and at the same time influences the performance of detectors. For this structure, the carrier concentration in the N_1-side should be as low as possible in order to avoid tunneling noise mechanism.

Based on our calculation, the result is obtained that except for the carrier concentration in the N_1-region, the other parameters such as the N_1-side surface recombination velocity S_p and width t_{N1} do not affect the detectivity, both of which via the N_1–n_2 interface recombination velocity S_{nn} change the detectivity. As above discussed, the quantum efficiency is mainly contributed by its component in the p-side, which determines that the parameters in the n-side including in the N_1 and n_2 regions do not change η. Therefore only R_0A influences D^*.

Fig. 9 shows the relation between S_p and S_{nn} with t_{N1} as a parameter. In the N_1–n_2 heterojunction, S_{nn} has a little increasing with S_p, which is completely different to S_{pp}. In addition, in the range of $S_p < 1$ m/s, t_{N1} almost does not influence S_{nn}. The result shows that S_p and t_{N1} could not have much influence on R_0A.

Fig. 10 shows the Auger and radiative mechanisms and their components in the n_2- and p-sides with the change of n_2. From Fig. 10, it is found that Auger and radiative noise mechanisms are mainly limited by their components in the p-region. The two noise mechanisms are caused by the minority carrier diffusion in the n- and p-type

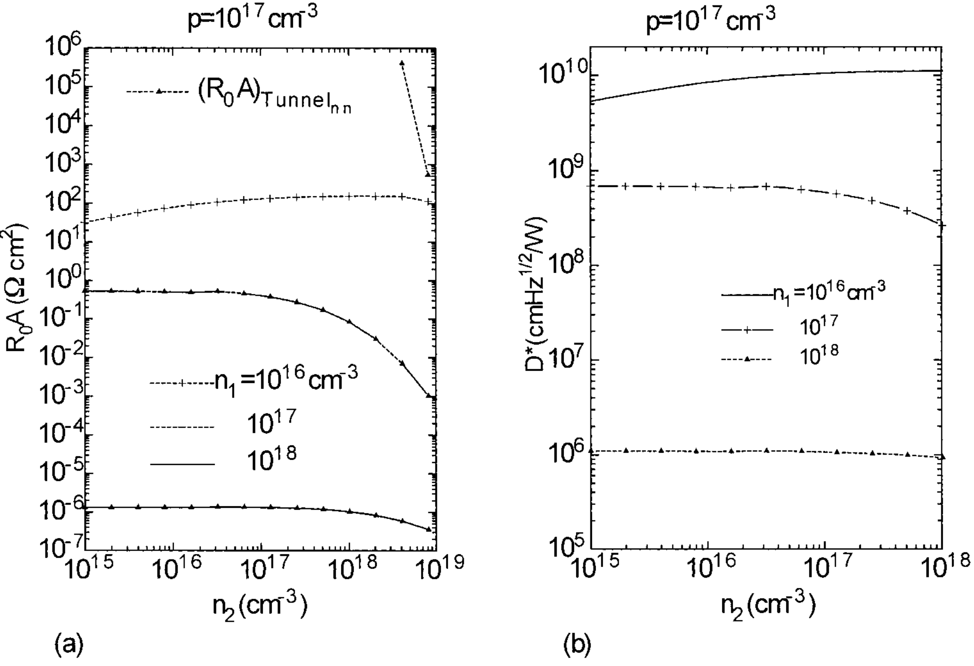

Fig. 8. The dependence of R_0A and D^* on the n_2-side carrier concentration (n_2) with the N_1-side carrier concentration (n_1) as a parameter operated at 300 K for the N_1–n_2–p structure

materials. In the n-type material, the diffusion length and lifetime for holes are lower than those for electrons in the p-type material, which determines that the diffusion current in the n-side is lower than that in the p-side, that is $J_{sn} < J_{sp}$. From Section 2, we know that $R_0A \propto 1/J_s$, which shows that Auger and radiative mechanisms in the p-side are the main noise mechanisms to limit $(R_0A)_{Auger}$ and $(R_0A)_{Rad}$, respectively. Therefore, the parameters in the n_2-side and related ones such as the N_1-side parameters do not influence R_0A.

From Fig. 7, it is known that R_0A is mainly limited by the GR noise mechanisms in

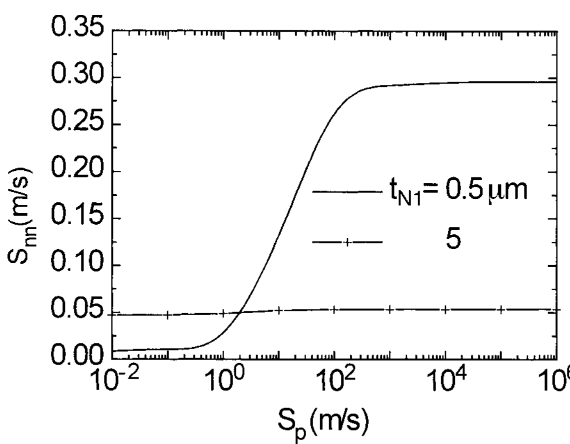

Fig. 9. The relation between the N_1–n_2 heterointerface recombination velocity (S_{nn}) and the N_1-side surface recombination velocity (S_p) with the N_1-side width (t_{N1}) as a parameter operated at 300 K

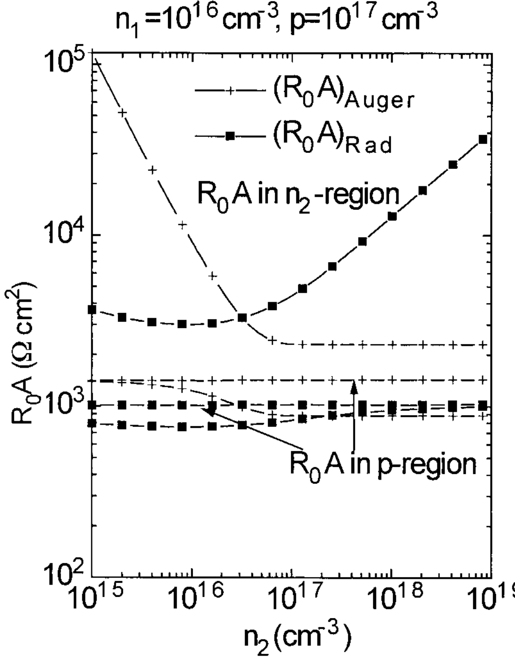

Fig. 10. The dependence of $(R_0A)_{\text{Auger}}$ and $(R_0A)_{\text{Rad}}$ as well as their components in the n_2- and p-regions on the n_2-side carrier concentration (n_2) operated at 300 K for the N_1–n_2–p structure

the n–p homojunction and N_1–n_2 heterojunction.

Due to the above three reasons, S_p and t_{N1} do not influence R_0A and therefore D^* is not changed with these two parameters.

Compared S_{pp} and S_{nn} with each other, it is found that, although the materials forming the N_1–n_2 and P_1–p_2 heterojunctions are the same, S_{pp} and S_{nn} are completely different with the different material types. S_{pp} at the P_1–p_2 heterojunction is much higher than S_{nn} at the N_1–n_2 heterojunction, which can be explained on the base of the expressions for S_{nn} and S_{pp}:

For S_{pp}, at $p_1 = 10^{16}\,\text{cm}^{-3}$ and $p_2 = 10^{17}\,\text{cm}^{-3}$, it is obtained by $L_{eP1} = 5.7 \times 10^2\,\mu\text{m}$, that is much larger than d_{P1} ($L_{eP1} \gg d_{P1}$), and $F(P_1)$ is approximated by $F(P_1) \approx r_{eP1} \approx L_{eP1}S_e/D_{eP1}$. Moreover, because $V_{dP1}(= 0.162\,\text{eV})$ is larger than ΔE_v ($-0.128\,\text{eV}$), S_{pp} should be expressed by $S_{pp} = (p_2D_{eP1}/p_1L_{eP1})\,F(P_1) \approx (p_2/p_1)S_e$. Therefore, except for the range of $S_e \to 0$ and $S_e \to \infty$, S_{pp} is linearly increasing with S_e as shown in Fig. 7; and because of $p_2 > p_1$, the relation $S_{pp} > S_e$ is obtained.

However, for S_{nn}, at $n_1 = 10^{16}\,\text{cm}^{-3}$ and $n_2 = 10^{18}\,\text{cm}^{-3}$, the value of V_{dN1} is 0.217 eV, which makes S_{nn} weakened exponentially. In addition, because of $L_{hN1} = 2.92\,\mu\text{m}$, $F(N_1)$ could not be approximated and the influence of S_p on S_{nn} is not distinct. Therefore, with the change of S_p, S_{nn} just has a little increasing.

Although the wide bandgap material GaSb is used to tailor the wavelength of the incident photons, which is convenient to select the working-wavelength, the P_1–p_2–n and N_1–n_2–p hetero- and homojunction structures do not show superiority compared with the n^+–n–p and p^+–p–n homojunction structures [12]. The carrier concentration in the wide bandgap material is limited to be a low value ($\approx 10^{16}\,\text{cm}^{-3}$) for both structures to avoid the tunneling noise, which is difficult to be obtained in the practical material growth. In addition, for the P_1–p_2 heterojunction, the heterointerface recombination velocity is not reduced but increased, which increases the Auger and radiative noise mechanisms and decreases the detectivity.

4. Conclusion

In this paper, the performance of the P_1–p_2–n and N_1–n_2–p hetero- and homojunction GaSb/$Ga_{0.8}In_{0.2}As_{0.19}Sb_{0.81}$ photodetectors is analyzed, based on the wavelength of the incident light and the parameters of GaSb and $Ga_{0.8}In_{0.2}As_{0.19}Sb_{0.81}$. The conclusions are drawn as follows:

(1) The absorption for the incident photons is mainly in the $Ga_{0.8}In_{0.2}As_{0.19}Sb_{0.81}$ p–n homojunction, especially in the p-type $Ga_{0.8}In_{0.2}As_{0.19}Sb_{0.81}$ material. The high detectivity is obtained with the photons first through the p-type $Ga_{0.8}In_{0.2}As_{0.19}Sb_{0.81}$ material, while the detectivity drops down with the photons first through the n-type $Ga_{0.8}In_{0.2}As_{0.19}Sb_{0.81}$ material. The wide bandgap material GaSb is used to tailor the wavelength.

(2) Although the absorption in GaSb does not appear, the parameters in GaSb also change the detectivity via the noise mechanisms and quantum efficiency component in $Ga_{0.8}In_{0.2}As_{0.19}Sb_{0.81}$. The high carrier concentration in GaSb strongly increases the tunneling noise mechanism and reduces the detectivity, either for the electrons through the N_1–n_2 heterojunction or for the holes through the P_1–p_2 heterojucntion.

(3) For p-type GaSb in the P_1–p_2–n structure, the high surface recombination velocity markedly reduces the detectivity via the P_1–p_2 heterointerface recombination velocity S_{pp} and the high width reduces the detectivity in the range of $S_e \to 0$ and improves the detectivity in the range of $S_e \to \infty$. On the contrary, for n-type GaSb in the N_1–n_2–p structure, the change of the surface recombination velocity and width almost do not influence the detectivity via S_{nn}. This result shows that, with the same condition for the N_1–n_2–p and P_1–p_2–n structures, the N_1–n_2–p structure is more advantageous than the P_1–p_2–n structure to obtain high detectivity.

Acknowledgement This paper is supported by the National Advanced Materials Committee of China (NAMCC).

Appendix A

A1 The noise mechanisms

The noise mechanisms can be divided into two parts. The one part is in the n–p homojunction, which has been analyzed in detail [11]. The other part is in the isotype heterojunction, where the effective interface recombination velocity S_{nn} or S_{pp}, located at the N–n or P–p heterojunction is introduced, which is derived from taking into account the minority carrier behavior in the N- or P-layer. Unlike anisotype heterojunction, the contribution of the minority carrier diffusion current embodied by the interface recombination velocity is neglected in the isotype heterojunctions. Therefore, only the GR and tunneling mechanisms are considered in isotype heterojunctions.

Based on the interface recombination velocity at the isotype homojunction [13] and the minority carrier diffusion in the anisotype heterojunction [14], S_{pp} and S_{nn} at the isotype heterojunctions are given by

$$S_{pp} = \begin{cases} \dfrac{p_2 D_{e_{p1}}}{p_1 L_{e_{p1}}} \exp\left(-(\Delta E_{v_{pp}} - qV_{d_{p1}})/KT\right) F(p_1) & V_{d_{p1}} < \Delta E_{v_{pp}} \\ \dfrac{p_2 D_{e_{p1}}}{p_1 L_{e_{p1}}} F(P_1) & V_{d_{p1}} > \Delta E_{v_{pp}} , \end{cases} \tag{A1}$$

$$F(\mathrm{P}_1) = \frac{\gamma_{\mathrm{e}_{\mathrm{p1}}} \cosh\left(\dfrac{d_{\mathrm{p1}}}{L_{\mathrm{e}_{\mathrm{p1}}}}\right) + \sinh\left(\dfrac{d_{\mathrm{p1}}}{L_{\mathrm{e}_{\mathrm{p1}}}}\right)}{\gamma_{\mathrm{e}_{\mathrm{p1}}} \sinh\left(\dfrac{d_{\mathrm{p1}}}{L_{\mathrm{e}_{\mathrm{p1}}}}\right) + \cosh\left(\dfrac{d_{\mathrm{p1}}}{L_{\mathrm{e}_{\mathrm{p1}}}}\right)}, \tag{A2}$$

$$S_{\mathrm{nn}} = \frac{n_2 D_{\mathrm{h}_{\mathrm{N1}}}}{n_1 L_{\mathrm{h}_{\mathrm{N1}}}} \exp\left(-qV_{\mathrm{d}_{\mathrm{N1}}}/KT\right) F(\mathrm{N}_1), \tag{A3}$$

$$F(\mathrm{N}_1) = \frac{\gamma_{\mathrm{p}_{\mathrm{N1}}} \cosh\left(\dfrac{t_{\mathrm{N1}}}{L_{\mathrm{p}_{\mathrm{N1}}}}\right) + \sinh\left(\dfrac{t_{\mathrm{N1}}}{L_{\mathrm{p}_{\mathrm{N1}}}}\right)}{\gamma_{\mathrm{p}_{\mathrm{N1}}} \sinh\left(\dfrac{t_{\mathrm{N1}}}{L_{\mathrm{p}_{\mathrm{N1}}}}\right) + \cosh\left(\dfrac{t_{\mathrm{N1}}}{L_{\mathrm{p}_{\mathrm{N1}}}}\right)}, \tag{A4}$$

where the build-in fields of $V_{\mathrm{d}_{\mathrm{P1}}}$ and $V_{\mathrm{d}_{\mathrm{N1}}}$ are in the wide bandgap materials at the isotype heterojunctions.

Because of the discontinuation of the energy band edges at the N–n and P–p heterojunctions, the GR current, which is related with the intrinsic carrier concentration and parameters in the depletion region [15,16], is divided into two parts,

$$J_{\mathrm{s}_{\mathrm{GR_c}}} = \frac{2KTn_{\mathrm{ic}} w_{\mathrm{c}} \sigma N_{\mathrm{f}}}{V_{\mathrm{d_c}}} \sqrt{\frac{3KT}{m_{\mathrm{c}}^*}}, \tag{A5}$$

where the subscript c represents the material type.

The tunneling mechanism at the heterointerface is the most important noise mechanism for detectors. The structure of $GaSb/Ga_{0.8}In_{0.2}As_{0.19}Sb_{0.81}$ forms a type II staggered heterojunction, where the potential barriers simultaneously separate both electrons and holes at both sides of the heteroboundary. If the barrier is sufficiently thin, the tunneling probability will markedly increase. A numerical model for tunneling across the heterointerface is presented by developing a thermionic-field emission boundary condition, which is formulated based on the WKB approximation [17]. For the $GaSb/Ga_{0.8}In_{0.2}As_{0.19}Sb_{0.81}$ isotype heterojunction, the electron tunneling in the conduction band for the N–n heterojunction and the hole tunneling in the valence band for the P–p heterojunction are considered in this paper. The tunneling current and the energy band profiles of N–n and P–p isotype heterojunctions are shown in Table 1, where the tunneling factors of P_{n} and P_{p} are given by

$$P_{\mathrm{n}} = \frac{\exp\left(\dfrac{E_{\mathrm{c}}(0^-)}{KT}\right)}{KT} \int_{E_{\min}}^{E_{\mathrm{c}}(0^-)} T(E_x) \exp\left(-\frac{E_x}{KT}\right) \mathrm{d}E_x, \tag{A6}$$

$$P_{\mathrm{p}} = \frac{\exp\left(-\dfrac{E_{\mathrm{v}}(0^+)}{KT}\right)}{KT} \int_{E_{\mathrm{v}}(0^+)}^{E_{\max}} T(E_x) \exp\left(\frac{E_x}{KT}\right) \mathrm{d}E_x \tag{A7}$$

with $T(E_x)$ the tunneling probability

$$T(E_x) = \left[-2 \int_{x_2}^{x_1} \sqrt{2m^* E_x} \frac{\mathrm{d}x}{\hbar} \right]. \tag{A8}$$

A2 The quantum efficiency

For the two structures, the light incident from the front- or backside surface is considered. Because of the thin width of the depletion region in the isotype heterojunction, the quantum efficiency is neglected in this region.

A2.1 Quantum efficiency in the N_1–n_2–p structure

On the base of Dhar's report for an n^+–n–p structure [18] and the photocurrent in the heterojunction [19], at a wavelength λ where the absorption coefficient is α, the quantum efficiency for the N_1–n_2–p heterostructure detector from N_1, n_2, p and anisotype junction depletion regions for the front- and backside illuminated cases is shown as follows.

a) Frontside illuminated case:

(1) Quantum efficiency in the p region

$$\eta_p = \frac{\alpha_p L_{e_p}}{\alpha_p^2 L_{e_p}^2 - 1} \left\{ \frac{\alpha_p L_{e_p} + r_e - e^{-\alpha_p(d_p - W_p)} \left[r_e \cosh\left(\frac{d_p - W_p}{L_{e_p}}\right) + \sinh\left(\frac{d_p - W_p}{L_{e_p}}\right) \right]}{r_e \sinh\left(\frac{d_p - W_p}{L_{e_p}}\right) + \cosh\left(\frac{d_p - W_p}{L_{e_p}}\right)} - \alpha_p L_{e_p} e^{-\alpha_p(d_p - W_p)} \right\} \tag{A9}$$

(2) Quantum efficiency in the depletion region

$$\eta_{dr} = \exp(-\alpha_p d_p) \left[\exp(\alpha_p W_p) - \exp(-a_{n2} W_n) \right] \tag{A10}$$

(3) Quantum efficiency in the n_2 region

$$\eta_{n2} = \frac{\alpha_{n2} L_{h_{n2}}}{\alpha_{n2}^2 L_{hn2}^2 - 1} \times \left[A \sinh\left(\frac{d_p + W_n}{L_{h_{n2}}}\right) + B \cosh\left(\frac{d_p + W_n}{L_{h_{n2}}}\right) + \alpha_{n2} L_{h_{n2}} \exp(-\alpha_p d_p - \alpha_{n2} W_n) \right], \tag{A11}$$

$$A = \frac{e^{-(\alpha_p d_p + \alpha_{n2} W_n)} - B \sinh\left(\frac{d_p + W_n}{L_{h_{n2}}}\right)}{\cosh\left(\frac{d_p + W_n}{L_{h_{n2}}}\right)}, \tag{A12}$$

$$B = \frac{(\gamma_{nn} - \alpha x_p)\exp(-\alpha x_p)\cosh\left(\frac{x_m}{L_{p_{n-}}}\right) - \exp(-\alpha x_m)\left[\sinh\left(\frac{x_p - x_m}{L_{p_{n-}}}\right) + \gamma_{nn}\cosh\left(\frac{x_p - x_m}{L_{p_{n-}}}\right)\right]}{\cosh\left(\frac{x_p - x_m}{L_{p_{n-}}}\right) + \gamma_{nn}\sinh\left(\frac{x_p - x_m}{L_{p_{n-}}}\right)} \tag{A13}$$

(4) Quantum efficiency in the N_1 region

$$\eta_{N1} = \frac{\alpha_{N1} L_{h_{N1}}}{\alpha_{N1}^2 L_{h_{N1}}^2 - 1} \times \left[C\sinh\left(\frac{d_p + t_{n2}}{L_{h_{N1}}}\right) + D\cosh\left(\frac{d_p + t_{n2}}{L_{h_{N1}}}\right) + \alpha L_{h_{N1}}\exp(-\alpha_p d_p - \alpha_{n2} t_{n2})\right], \tag{A14}$$

$$C = \frac{(\gamma_p - \alpha_{N1} L_{h_{N1}})\,e^{(-\alpha_p d_p - \alpha_{n2} t_{n2} - \alpha_{N1} t_{N1})} - D\left[\cosh\left(\frac{d_p + t_{n2} + t_{N1}}{L_{h_{N1}}}\right) + \gamma_p\sinh\left(\frac{d_p + t_{n2} + t_{N1}}{L_{h_{N1}}}\right)\right]}{\left[\gamma_p\cosh\left(\frac{d_p + t_{n2} + t_{N1}}{L_{h_{N1}}}\right) + \sinh\left(\frac{d_p + t_{n2} + t_{N1}}{L_{h_{N1}}}\right)\right]}, \tag{A15}$$

$$D = \frac{\left[\begin{array}{c} e^{(-\alpha_p d_p - \alpha_{n2} t_{n2})}(\gamma_{nn} - \alpha_{N1} L_{h_{N1}})\left[\sinh\left(\frac{d_p + t_{n2} + t_{N1}}{L_{h_{N1}}}\right) + \gamma_p\cosh\left(\frac{d_p + t_{n2} + t_{N1}}{L_{h_{N1}}}\right)\right] - \\ -e^{(-\alpha_p d_p - \alpha_{n2} t_{n2} - \alpha_{N1} t_{N1})}(\gamma_p - \alpha_{N1} L_{h_{N1}})\left[\sinh\left(\frac{d_p + t_{n2}}{L_{h_{N1}}}\right) + \gamma_{nn}\cosh\left(\frac{d_p + t_{n2}}{L_{h_{N1}}}\right)\right] \end{array}\right]}{\left[\gamma_p\cosh\left(\frac{t_{N1}}{L_{h_{N1}}}\right) + \sinh\left(\frac{t_{N1}}{L_{h_{N1}}}\right)\right] - \gamma_{nn}\left[\cosh\left(\frac{t_{N1}}{L_{h_{N1}}}\right) + \gamma_p\sinh\left(\frac{t_{N1}}{L_{h_{N1}}}\right)\right]} \tag{A16}$$

b) Backside illuminated case:

(1) Quantum efficiency in the N_1 region

$$\eta_{N1} = \frac{\alpha_{N1} L_{h_{N1}}}{\alpha_{N1}^2 L_{h_{N1}}^2 - 1}\left[A\sinh\left(\frac{t_{N1}}{L_{h_{N1}}}\right) + B\cosh\left(\frac{t_{N1}}{L_{h_{N1}}}\right) + \alpha_{N1} L_{h_{N1}}\exp(-\alpha_{N1} t_{N1})\right], \tag{A17}$$

$$B = \gamma_p A - (\gamma_p + \alpha_{N1} L_{h_{N1}}), \tag{A18}$$

$$A = \frac{(\gamma_p + \alpha_{N1} L_{h_{N1}})\left[\cosh\left(\frac{t_{N1}}{L_{h_{N1}}}\right) - \gamma_{nn}\sinh\left(\frac{t_{N1}}{L_{h_{N1}}}\right)\right] - e^{(-\alpha_{N1} t_{N1})}(\gamma_{nn} + \alpha_{N1} L_{h_{N1}})}{\left[\gamma_p\cosh\left(\frac{t_{N1}}{L_{h_{N1}}}\right) + \sinh\left(\frac{t_{N1}}{L_{h_{N1}}}\right)\right] - \gamma_{nn}\left[\cosh\left(\frac{t_{N1}}{L_{h_{N1}}}\right) + \gamma_p\sinh\left(\frac{t_{N1}}{L_{h_{N1}}}\right)\right]} \tag{A19}$$

(2) Quantum efficiency in the n_2 region

$$\eta_{n2} = \frac{\alpha_{n2} L_{h_{n2}}}{\alpha_{n2}^2 L_{h_{n2}}^2 - 1}\left[C\sinh\left(\frac{t_{N1} + t_{n2} - W_n}{L_{h_{n2}}}\right) - D\cosh\left(\frac{t_{N1} + t_{n2} - W_n}{L_{h_{n2}}}\right) - \alpha_{n2} L_{h_{n2}}\,e^{[-\alpha_{N1} t_{N1} - \alpha_{n2}(t_{n2} - W_n)]}\right], \tag{A20}$$

$$C = \frac{D \sinh\left(\frac{t_{N1} + t_{n2} - W_n}{L_{h_{n2}}}\right) - e^{[-\alpha_{N1} t_{N1} - \alpha_{n2}(t_{n2} - W_n)]}}{\cosh\left(\frac{t_{N1} + t_{n2} - W_n}{L_{h_{n2}}}\right)}, \tag{A21}$$

$$D = \frac{e^{[-\alpha_{N1} t_{N1} - \alpha_{n2}(t_{n2} - W_n)]}\left[\gamma_{nn} \cosh\left(\frac{t_{N1}}{L_{h_{n2}}}\right) - \sinh\left(\frac{t_{N1}}{L_{h_{n2}}}\right)\right] - (\gamma_{nn} + \alpha_{n2} L_{h_{n2}})\, e^{-\alpha_{N1} t_{N1}} \cosh\left(\frac{t_{N1} + t_{n2} - W_n}{L_{h_{n2}}}\right)}{\cosh\left(\frac{t_{n2} - W_n}{L_{h_{n2}}}\right) + \gamma_{nn} \sinh\left(\frac{t_{n2} - W_n}{L_{h_{n2}}}\right)}. \tag{A22}$$

(3) Quantum efficiency in the p region

$$\eta_p = \frac{\alpha_p L_{e_p}}{\alpha_p^2 L_{e_p}^2 - 1} e^{(-\alpha_{N1} t_{N1} - \alpha_{n2} t_{n2} - \alpha_p W_p)} \times \left\{ \alpha_p L_{e_p} - \frac{(\alpha_p L_{e_p} - r_e)\, e^{-\alpha_p (d_p - W_p)} + \left[r_e \cosh\left(\frac{d_p - W_p}{L_{e_p}}\right) + \sinh\left(\frac{d_p - W_p}{L_{e_p}}\right)\right]}{r_e \sinh\left(\frac{d_p - W_p}{L_{e_p}}\right) + \cosh\left(\frac{d_p - W_p}{L_{e_p}}\right)} \right\}. \tag{A23}$$

(4) Quantum efficiency in the depletion region

$$\eta_{dr} = e^{[-\alpha_{N1} t_{N1} - \alpha_{n2}(t_{n2} - W_n)]} - e^{(-\alpha_{N1} t_{N1} - \alpha_{n2} t_{n2} - \alpha_p W_p)}. \tag{A24}$$

A2.2 Quantum efficiency in the P_1–p_2–n structure

The expressions of the quantum efficiency for the P_1–p_2–n structure with the front- and backside illuminated cases are the same as those in the N_1–n_2–p structure. However, the parameters in the N_1–n_2–p structure should be exchanged to the corresponding ones in the P_1–p_2–n structure, which are shown below,

$$N_1 \to P_1, \quad L_{h_{N1}} \to L_{e_{P1}}, \quad \alpha_{N1} \to \alpha_{P1},$$

$$t_{N1} \to d_{P1}, \quad \gamma_e \to \gamma_p, \quad \gamma_{nn} \to \gamma_{pp},$$

$$n_2 \to p_2, \quad \alpha_{n2} \to \alpha_{p2}, \quad L_{h_{n2}} \to L_{e_{p2}}, \quad t_{n2} \to d_{p2}, \quad W_n \to W_p,$$

$$\alpha_p \to \alpha_n, \quad W_p \to W_n, \quad p \to n, \quad L_{e_p} \to L_{h_n}, \quad \gamma_e \to \gamma_p, \quad d_p \to t_n.$$

The parameters before arrows are the ones in the P_1–p_2–n structure and those after arrows are the ones in the N–p_2–p_1 structure.

In the expression of quantum efficiency, the absorption coefficients of the n- and p-type $Ga_{0.8}In_{0.2}As_{0.19}Sb_{0.81}$ material are the same.

Appendix B

Notation

S_p = surface recombination velocity in n-type material
S_e = surface recombination velocity in p-type material

S_{pp} = interface recombination velocity in the p_1–p_2 heterojunction
S_{nn} = interface recombination velocity in the n_1–n_2 heterojunction
W_{nn} = width of the depletion region in the n_1–n_2 heterojunction
W_{np} = width of the depletion region in the n–p heterojunction
W_{pp} = width of the depletion region in the p_1–p_2 heterojunction
W_n = width of the depletion region in the n-type material
W_p = width of the depletion region in the p-type material
n = electron carrier concentration in the n-type material
p = hole carrier concentration in the p-type material
$\Delta E_{c_{nn}}$ = conduction band discontinuity at the n_1–n_2 heterointerface
$\Delta E_{v_{nn}}$ = valence band discontinuity at the n_1–n_2 heterointerface
$\Delta E_{c_{pp}}$ = conduction band discontinuity at the p_1–p_2 heterointerface
$\Delta E_{v_{pp}}$ = valence band discontinuity at the p_1–p_2 heterointerface
D_e = Electron diffusion coefficient in the p-type material
L_e = electron diffusion length in the p-type material
D_h = hole diffusion coefficient in the n-type material
L_h = hole diffusion length in the n-type material
δ = Fermi energy level
V_{dn} = built-in field in the n-type material
V_{dp} = built-in field in the p-type material
α_p = absorption coefficient in the p-type material
α_n = absorption coefficient in the n-type material
t = width of the n-type material
d = width of the p-type material
σ = trap capture cross section
N_f = trap density
K = Boltzmann's constant
T = detector working temperature
q = electronic charge
E_g = material energy bandgap
A^* = $4\pi m^* q K^2/h^3$ effective Richardson constant
m^* = effective mass

References

[1] A. Rogalski and M. Razeghi, SPIE **3287**, 2 (1998).
[2] A.Z. Shellenbarger, G.M. Mauk, I.M. Gottfried, D.J. Lesko, and L.C. Di Netu, SPIE **2999**, 25 (1997).
[3] H.K. Choi, C.A. Wang, G.W. Turne, and M.J. Manfra, Appl. Phys. Lett. **77**, 3758 (1997).
[4] J.M. Arias, J.G. Pasko, L.J. Kozlowski, and R.E. DeWames, Opt. Engng. **33**, 1422 (1994).
[5] C. Musca, J. Antoszewski, J. Dell, L. Faraone, J. Piotrowski, and Z. Nowak, J. Electron. Mater. **27**, 470 (1998).
[6] M.H. Weler and G.J. Turnowski, J. Electron. Mater. **26**, 635 (1997).
[7] Z. Shellenbarger, M. Mauk, J. Cox, J. South, J. Lesko, P. Sims, M. Jhabvala, and M.K. Fortin, SPIE **3287**, 138 (1998).
[8] J.D. Kim, E. Michel, H. Mohseini, J. Wojkowski, J.J. Lee, and M. Razeghi, SPIE **2999**, 55 (1997).
[9] Y. Tian, T. Zhou, B. Zhang, Y. Jin, Y. Ning, H. Jiang, and G. Yuang, Opt. Engng. **37**, 1754 (1998).
[10] Y. Tian, T. Zhou, B. Zhang, H. Jiang, and Y. Jin, Solid State Electron. **43**, 625 (1999).

[11] Y. TIAN, T. ZHOU, B. ZHANG, H. JIANG, and Y. JIN, J. Phys. D **31**, 3291 (1998).
[12] Y. TIAN, T. ZHOU, B. ZHANG, H. JIANG, and Y. JIN, Solid State Electron., to be published.
[13] J. ALAMO, J. MEERBERGEN, F. D'HOOR, and J. NIJS, Solid State Electron. **24**, 533 (1981).
[14] M.A. STETTLER and M.S. LUNDSTROM, IEEE Trans. Electron. Device **ED-41**(4), 592 (1994).
[15] D.L. SMITH, phys. stat. sol. (a) **44**, 381(1977).
[16] A. ROGALSIK, Infrared Phys. **28**, 139 (1988).
[17] K. YANG, J. EAST, and G. HADDAD, Solid State Electron. **36**, 321 (1991).
[18] V. DHAR and R. ASHOKAN, Semicond. Sci. Technol. **12**, 580 (1997).
[19] B.L. SHARM and R.K. PUROHIT, Semiconductor Heterojunction, 1974.